Quantum Hall Dual-Band Infrared Photodetector

Chiu-Chun Tang,[1] K. Ikushima,[2] D. C. Ling,[3] C. C. Chi,[1] and Jeng-Chung Chen[1]
[1]*Department of Physics, National Tsing Hua University, Hsinchu 30013, Taiwan*
[2]*Department of Applied Physics, Tokyo University of Agriculture and Technology, Koganei, Tokyo 184-8588, Japan*
[3]*Department of Physics, Tamkang University, Tamsui District, New Taipei City 25137, Taiwan*
(Received 25 May 2017; revised manuscript received 11 September 2017; published 1 December 2017)

We have developed a hybrid quantum Hall midinfrared (QHMIR)–quantum Hall far-infrared (QHFIR) photodetector by the use of graphene-GaAs/(Al, Ga)As–layered composite material. Both MIR and FIR photoresistance are observed in a single chip by utilizing cyclotron resonance in the quantum Hall regimes of graphene and two-dimensional electron gas (2DEG) in GaAs/(Al, Ga)As heterostructure, respectively. By cooperatively operating 2DEG as a back-gate electrode to change the carrier density of graphene or graphene as a top-gate electrode to modulate the carrier density of 2DEG with an applied gate voltage less than 1 V and applying the magnetic field to tune cyclotron resonance, we achieve a wide frequency selectivity, covering 640–790 cm^{-1} for the graphene-QHMIR detector and 24–89 cm^{-1} for the 2DEG-QHFIR detector. Moreover, our design integrates a log-periodic antenna with the detector to minimize the device size, while preserving high sensitivity. Our results pave the way for implementing a highly tunable MIR-to-FIR photodetector and a dual-band (MIR-FIR) imaging array.

DOI: 10.1103/PhysRevApplied.8.064001

I. INTRODUCTION

Indefatigable research efforts in infrared (IR) technologies to develop and exploit advanced IR detectors for fundamental research and applications have persisted for decades [1]. An ultimate IR detector should possess high responsivity R_v, low noise-equivalent power (NEP), high and tunable specific detectivity D^*, and preferably higher operating temperatures. Nevertheless, the trade-off among these figures of merit in various types of IR detectors—mostly due to material limitations—always has to be considered in practical use.

Quantum Hall infrared (QHIR) detectors based on cyclotron resonance (CR) of two-dimensional electron gas (2DEG) are known to be very sensitive and frequency selectable [2,3]. For example, typical QHIR detectors made of GaAs-based 2DEG have been reported for operation at the far-infrared (FIR) band of $27-102\ cm^{-1}$, tuned by external magnetic field B [4]. The optimal performance of the QHFIR photodetector has been achieved with a high R_v of $\sim 10^8$ V/W and a NEP of $\leq 10^{-14}$ $W/Hz^{1/2}$ at 4.2 K [2]. Recent advances in the search of cooling technologies and novel low-dimensional materials significantly foster the implementation of QHFIR detectors and enrich their detection spectrum. First, nowadays, refrigeration has become more accessible due to the invention of cryogen-free systems [5]. Second, distinct quantum Hall states (QHSs) in various low-dimensional materials with different CR frequencies, such as graphene [6], atomically thin black phosphorus [7], topological insulators [8], and 2DEG at oxide interfaces [9] have been recently discovered and shed new light on developing innovative photodetectors. Therefore, it is conceptually feasible to implement a hybrid QHIR detector by stacking conventional semiconductor heterostructures and one of the new 2D materials to achieve a wide spectra range of photodetection. To date, however, the attention of such research has not been geared towards this aspect [10].

In this work, we implement a hybrid quantum Hall detector by stacking graphene on GaAs/(Al, Ga)As heterostructure embedded with 2DEG, as illustrated in Fig. 1(a), where a 2DEG layer and graphene are capacitively coupled. Graphene has attracted a great deal of attention for constructing innovated optoelectronics due to its high carrier mobility [11], broad absorption spectrum [12], and high thermal sensitivity [10]. In addition, graphene and GaAs-2DEG hold distinctly different Landau-level (LL) energies: $E_N^{\rm gr} = {\rm sgn}(N) v_F \sqrt{2e\hbar B|N|}$ for graphene and $E_n^{\rm 2D} = (n+1/2)\hbar\omega_c^{\rm 2D}$ for 2DEG, where v_F is the Fermi velocity of graphene, $\hbar$ is Planck's constant, N and n are Landau-level indices of graphene and 2DEG, respectively, $\omega_c^{\rm 2D} = eB/m^*$ is the cyclotron frequency of 2DEG with the effective mass m^* ($\sim 0.067 m_0$, where m_0 is the free-electron mass), and B is the magnetic field perpendicular to the sample surface. Figure 1(b) shows $E_n^{\rm 2D}$ and $E_N^{\rm gr}$ as a function of B. It can be readily seen that at $B = 8$ T, the first LL energy spacing for graphene is $\Delta E^{\rm gr} = \hbar\omega_c^{\rm gr} = v_F\sqrt{2e\hbar B}(\sqrt{N+1}-\sqrt{N}) \sim 100$ meV (for $N = 0 \rightarrow 1$), and $\Delta E^{\rm 2D} \sim 25$ meV, which corresponds to the photon frequency f in the midinfrared (MIR) and far-infrared (FIR) range, respectively. Because of a large discrepancy in CR frequency between 2DEG and graphene, the photoresponse of the two materials is expected to be observed at different IR bands. Consequently, the combination of graphene and 2DEG provides a platform to realize

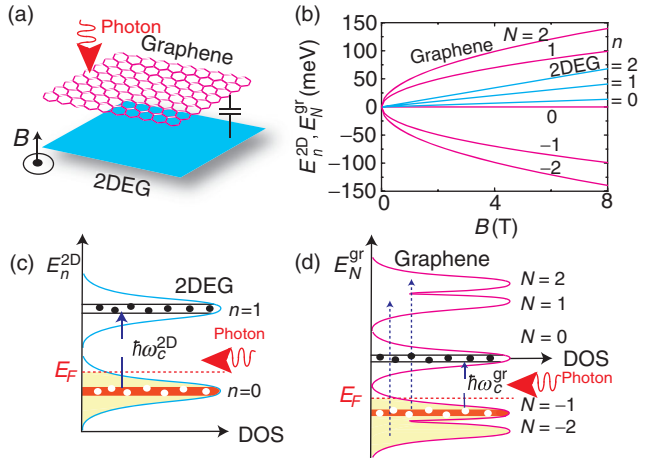

FIG. 1. (a) Schematic configuration of a graphene–GaAs-2DEG capacitively coupled bilayer system. (b) Plot of the Landau-level (LL) energy E_N^{gr} of graphene and E_n^{2D} of GaAs-2DEG as a function of the magnetic field B for Landau index $N = 0, \pm1, \pm2$ and $n = 0, 1, 2$, respectively. Schematic diagram of the LL density of states (DOSs) of (c) GaAs-2DEG and (d) graphene. Extended and localized states are represented by bright and dark colors, respectively. Energy levels are broadening in the presence of disorder. When the photon energy matches LL energy spacing, electron-hole pairs are generated, giving rise to a measurable photoresponse.

a quantum Hall midinfrared (QHMIR)–quantum Hall far-infrared (QHFIR) dual-band detector.

II. PHOTON-DETECTION PRINCIPLE

The underlying mechanism of the detection scheme for the QHIR detector has been well established [2,3]. The photoresponse can be attributed to the nonresonance effect and CR absorption [3]. Since the nonresonance effect is not a well-controlled experimental parameter, we intend to focus on the CR effects in the device design. When the illuminating photon energy matches the LL energy spacings of 2DEG and graphene, electrons and holes are excited via CR absorption. Schematic representations of the photoexcitation process on 2DEG and graphene are illustrated in Figs. 1(c) and 1(d), respectively. These nonequilibrium photoexcited carriers cause charges to build up along the edge of the Hall bar, yielding a detectable change in the longitudinal resistance ΔR_{sig} [2,3]. The performance of the GaAs-2DEG QHFIR detector has been well studied; in contrast, that of graphene the QHMIR detector is much less explored. The selection rule for the photon absorption processes follows $\Delta n = \pm1$ for GaAs-2DEG and $\Delta|N| = \pm1$ for graphene. The QHSs of graphene have been demonstrated to be sensitive to the MIR photon with a frequency ranging from 1100 to 25 cm^{-1} [13]. Both intraband and interband transitions are allowed in the photon absorption process for graphene [14]; nevertheless, the intraband transition between adjacent LLs is easier to observe in the experiment [15,16]. Because the energy gaps for $N = 0 \to 1$ and $N = -1 \to 0$ transitions are the largest, they are expected to be more robust against LL broadening due to the presence of disorder. We, therefore, consider that the photon absorption between $N = 0$ and ±1 are the dominant processes in graphene-QHMIR photoresponse.

III. DEVICE CONCEPT AND CHARACTERIZATION

The layout of the hybrid QHMIR-QHFIR detector investigated in our experiment is schematically shown in Fig. 2(a). The device consists of a chemical-vapor-deposited (CVD) graphene, a GaAs/$Al_{0.3}Ga_{0.7}As$ single heterostructure with 2DEG 90 nm beneath, a log-periodic antenna (LPA), and an ionic liquid coated on graphene as a top-gate electrode. Our design aims to increase frequency

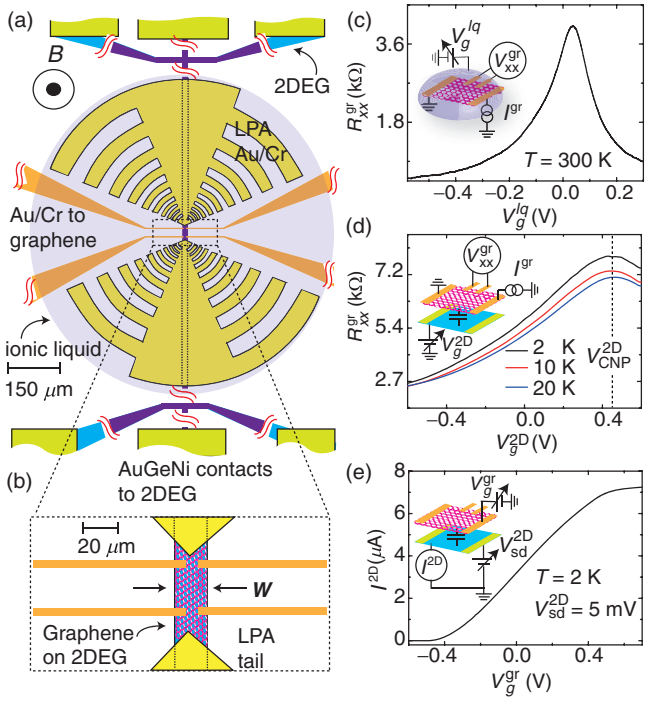

FIG. 2. (a) Schematic layout (in scale with the real device) of the quantum Hall dual-band photodetector by use of graphene-GaAs/(Al, Ga)As heterostructure composite material. The hybrid device consists of GaAs-2DEG, graphene, metal contacts for the gate and source-drain electrodes, log-periodic antenna, and ionic liquid. (b) Enlarged view of the photosensitive area. (c) Four-terminal longitudinal resistance of the graphene R_{xx}^{gr} as a function of the voltage V_g^{lq} applied to the ionic-liquid gate at room temperature ($T = 300$ K). (d) R_{xx}^{gr} as a function of the voltage V_g^{2D} applied to the 2DEG gate at $T = 2$, 10, and 20 K with $V_g^{lq} = 0$ V. The black dashed line denotes the charge neutral point (CNP) of graphene at $V_{CNP}^{2D} = 0.46$ V. (e) Current I^{2D} through 2DEG versus the voltage V_g^{gr} applied to the graphene gate at $T = 2$ K and $V_g^{lq} = 0$ V. The insets in (c) to (e) show the measurement circuitries.

selectivity and have a miniature chip for the hybrid device, as described in the details below.

One of the important merits of the QHIR detector is its excellent wavelength selectivity, which is achieved by varying CR frequency via sweeping B [2,13]. To fully exploit this property, the carrier density can be served as another knob to tune QHSs. Our early study has shown that graphene and 2DEG layer can function as a mutual channel material and gate electrode for each other to facilitate the dual-function electric-field effect [17]. For the QHFIR detector, we have also demonstrated that graphene can be used as a transparent top gate to tune the carrier density n^{2D} of 2DEG, yielding a wide detection range of 27–102 cm^{-1} [4]. For QHMIR operation, applying a bias voltage at 2DEG back gate to tune the carrier density n^{gr} of graphene is viable, but its maximum gating range is limited by the interface band bending in the GaAs/(Al, Ga)As heterostructure [17]. To remedy this drawback, we employ a solid polymer electrolyte, composed of polyethylene oxide and $LiClO_4$—a commonly used ionic liquid [18]—onto graphene. The ion-gel gate is operable above $T \sim 250$ K and can electrically dope graphene to very high $n^{gr}(\sim 10^{13}\ cm^{-2})$ [19]. We have measured FIR-MIR transmission spectra of the ionic liquid by using Fourier transform infrared spectroscopy (FTIR) and found no evident response within the infrared frequency range of 40–650 cm^{-1}, which is consistent with previous work [20]. As a result, this design allows us to expand the tuning capability of n^{gr} by cooperatively manipulating the ion-gel gate and the 2DEG gate. The operating scheme is as follows: we first bias the ion-gel gate to tune n^{gr} to the desired regime at room temperature, cool down the detector, and then use the 2DEG gate to fine-tune n^{gr} at low temperatures.

The other important goal in the present work is to minimize the chip size for potential applications in the imaging array. It has been recognized that ΔR_{sig} of a QHIR detector can be effectively enhanced by increasing the aspect ratio (length L to width W) of the device [2]. As a rule of thumb, conventional QHFIR detectors are commonly patterned into a very long Hall bar, e.g., $L\sim$ several centimeters [2,4,21]. The long QHFIR detector, however, cannot efficiently couple IR radiation with the 2DEG because of impedance mismatch. To retain decent photoresponse in a detector with a reduced size, we employ a LPA to couple FIR-MIR into the detection area and to polarize the electric field along the channel direction [22]. The diameter of the largest and the smallest segments of the LPA is 375 and 32 μm, respectively. The LPA is expected to resonate from 0.1 THz ($\sim$3.3 cm^{-1}) to 1.1 THz ($\sim$36.3 cm^{-1}). The end of the LPA is tapered into a bow-tie-like structure to focus radiation with a shorter wavelength.

We now proceed to describe the details of the device fabrication procedure. The CVD-grown graphene was transferred onto a GaAs/(Al, Ga)As heterostructure, on which the ohmic contacts made of (Au,Ge)Ni alloy for 2DEG have been prepatterned. The details of the growth, transfer, lithography procedures, and characterizations of the CVD graphene are referred to in our previous publications [17,23]. Care has been taken to ensure that the graphene is electrically isolated from the contact metals for 2DEG. We then define the graphene-2DEG mesa into a Hall-bar geometry with $W = 20$ μm and $L = 1$ mm in a self-aligned manner. Subsequently, Au/Cr (30 nm/5 nm) metal layers are deposited onto the graphene, serving as antenna and electrode materials for electrical measurements. Finally, ionic liquid is dropped onto the graphene surface as a gate electrode. The center gap of the LPA defines the exact sensing area A_s, $\sim 90 \times 20$ μm^2. The size of the LPA is much larger than A_s and limits the minimum chip size.

Figures 2(c)–2(e) demonstrate full electric characteristics of the investigated hybrid device. We characterize n^{2D}, n^{gr}, and the mobility of 2DEG μ^{2D} and graphene μ^{gr} at 4.2 K: $n^{2D} = 2.5 \times 10^{11}\ cm^{-2}$, $n^{gr} = 3.3 \times 10^{11}\ cm^{-2}$, $\mu^{2D} = 9.8 \times 10^5\ cm^2/Vs$, and $\mu^{gr} = 3540\ cm^2/Vs$. The measurement circuits are shown in the insets of Figs. 2(c)–2(e) for different operations, as explained below. Here, we denote gate voltages on the graphene gate, the ion-gel gate, and the 2DEG gate as V_g^{gr}, V_g^{lq}, and V_g^{2D}, respectively. Figure 2(c) displays the four-terminal resistance of graphene R_{xx}^{gr} as a function of V_g^{lq} at room temperature ($T = 300$ K). The maximum R_{xx}^{gr} corresponds to the position of the charge neutral point (CNP). Figure 2(d) shows R_{xx}^{gr} versus V_g^{2D} at $T = 2$, 10, 20 K with $V_g^{lq} = 0$ V. The CNP of graphene is located at $\sim$0.46 V ($= V_{CNP}^{2D}$). We can estimate $n^{gr}(V_g^{2D})$ by using $n^{gr}(V_g^{2D}) = C_{GaAs}(V_g^{2D}\text{-}V_{CNP}^{2D})/e$, where $C_{GaAs}(\approx 130\ nF/cm^2)$ is the capacitance between graphene and 2DEG [17]. To demonstrate the electric tunability of n^{2D} by the use of the graphene gate, Fig. 2(e) plots current I^{2D} through 2DEG versus V_g^{gr} with a bias voltage V_{sd}^{2D} of 5 mV applied on 2DEG. We can see that n^{2D} is depleted as $V_g^{gr} \sim -0.43$ V. In the other end, n^{2D} is increased up to $5.2 \times 10^{11}\ cm^{-2}$ as $V_g^{gr} \sim 0.54$ V, deduced from the measurement of the QHSs.

Broadband blackbody radiation at 800 °C chopped at 21 Hz is used as a weak IR source and is guided down to the cryostat by a copper hollow pipe [24]. A manually controllable optical shutter located in front of the detector at low temperatures is implemented for checking the photoresponse of the detector. Both the incident radiation and the applied magnetic field are set to be normal to the sample surface (Faraday geometry).

IV. RESULTS AND DISCUSSION

We first demonstrate the performance of the hybrid device as a QHFIR detector. The device is driven by a dc current $I^{2D} = 1$ μA through the 2DEG channel, and the photoresponse defined as $\Delta R_{sig}^{2D}(= \Delta V_{xx}^{2D}/I^{2D})$ is

measured using a standard lock-in technique. The circuitry for QHFIR measurement is illustrated in the upper-left inset of Fig. 3(a). Figure 3(a) shows R_{xx}^{2D} (black dashed line) and ΔR_{sig}^{2D} (red solid line) of 2DEG as a function of B at $V_g^{gr} = 0$ V. For reference, the corresponding cyclotron frequency is indicated in the upper scale of Fig. 3(a), where the positions for integer filling factors ν^{2D} $(= hn^{2D}/eB)$ are indicated by the arrows. The transition regions of QHSs are marked by the gray areas, wherein photoresponses due to CR absorption are properly observed. The photosignals outside the gray regime are attributed to nonresonant effects [3]. When the shutter blocks the light illumination, all photosignals disappear [24]. The photosignal modulation $(\Delta R_{sig}^{2D}/R_{xx}^{2D})$ at $\nu^{2D} \sim 4$ is approximately 0.5%, which is much larger than ~0.01% of typical QHFIR detectors without LPA [4,21]. The presence of the LPA significantly enhances the photoresponse at $\nu^{2D} > 6$, consistent with previous report [22]. Early studies by using a Fourier transform spectrometer have shown that the spectra of ΔR_{sig}^{2D} match well with CR transmission spectra [21]. Therefore, in principle, the frequency range of detection can be selected by picking up the photoresponse from different QHSs. Figures 3(b) and 3(c) show two representative traces of photoresponse at $\nu^{2D} \sim 4.5$ and ~2.7 for V_g^{gr} decreasing from 0.4 V to −0.1 V as a function of B, respectively. It is found that for a given ν^{2D}, the photoresponse shifts to the lower-frequency regime with decreasing n^{2D}. Within the applied voltage range of V_g^{gr}, the frequency range of FIR detection covers from ~25 cm^{-1} to ~100 cm^{-1}, which are comparable to our previous report, obtained from a rather long QHFIR with $L = 5.3$ cm [4]. By comparing the photoresponse of our QHFIR detector with that of a calibrated bolometer, the R_v is estimated to be $\sim 8.2 \times 10^4$ V/W. The NEP of the detector, determined from the noise level on the ΔR_{sig}^{2D} peaks, is around 1.4×10^{-11} W/$Hz^{1/2}$ (with 3 Hz bandwidth) [2,3].

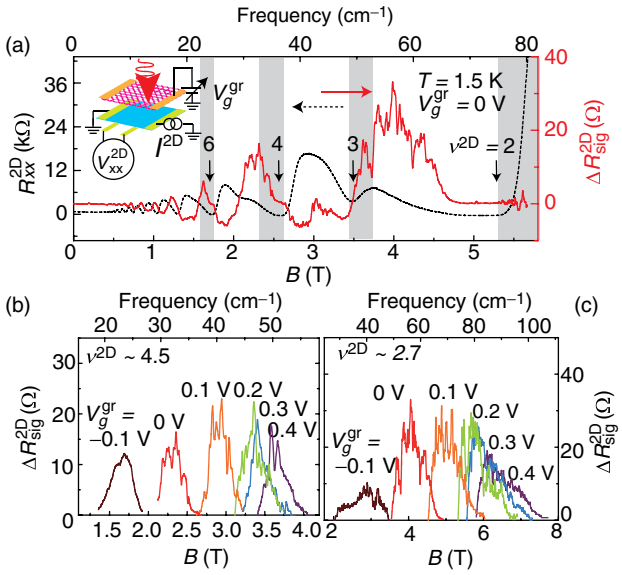

FIG. 3. (a) The magnetoresistance R_{xx}^{2D} (dashed line) and photoresponse ΔR_{sig}^{2D} (solid line) of the QHFIR detector as a function of B at 1.5 K. The upper-left schematics shows the measurement setup. The shaded areas marked with integers correspond to the QHS regimes of the 2DEG with its integer filling factors ν^{2D}. ΔR_{sig}^{2D} at (b) $\nu^{2D} \sim 4.5$ and (c) $\nu^{2D} \sim 2.7$ as a function B at various V_g^{gr} from 0.4 V to −0.1 V in a step of $\Delta V_g^{gr} = -0.1$ V. The corresponding cyclotron frequency is indicated in the upper scale.

In the following, we turn to present the characterization and the photoresponse of the hybrid device through graphene channel as a QHMIR detector. Figure 4(a) shows R_{xx}^{gr} as a function of $V_g^{2D} - V_{CNP}^{2D}$ at 2 K for various B. The cone shape of R_{xx}^{gr} shown in Fig. 2(d) gradually evolves into a valley and a second peak as B goes beyond 5 T. The evolution of R_{xx}^{gr} with V_g^{2D} and B indicates that graphene is driven into the QH regime. The emergence

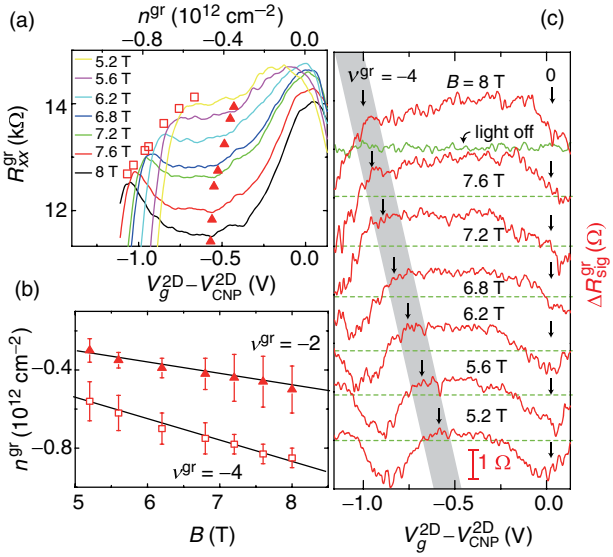

FIG. 4. Device characterization and performance for QHMIR detector (a) Graphene magnetoresistance R_{xx}^{gr} versus V_g^{2D}-V_{CNP}^{2D} for various B at 2 K, measured with $I^{gr} = 0.5$ μA. The hollow squares and solid triangles indicate the evolutions of the peak and the valley of R_{xx}^{gr} with B, respectively. These features can be resolved as $B > 5$ T. (b) The B dependence of n^{gr} extracted from the data of the hollow squares and solid triangles in (a). For comparison, the fitted solid lines indicate n^{gr} associated with filling factor $\nu^{gr}(= hn^{gr}/eB) = -2$ and −4. (c) The photoresponse ΔR_{sig}^{gr} as a function of V_g^{2D}-V_{CNP}^{2D} for various B at 2 K. The traces have been shifted for clarity. When the optical shutter is closed, the key features on ΔR_{sig}^{gr} disappear, as shown in the green trace at $B = 8$ T. This dark photoresponse is presented by the green dashed lines for the rest traces. The arrows indicate the positions of $\nu^{gr} = -4$ and zero (at $V_g^{2D} = V_{CNP}^{2D}$). The shaded area covered $\nu^{gr} \sim -4$ indicates the regime where CR absorption of graphene is justified (see Ref. [25] and main text for details).

of the R_{xx}^{gr} valley marked by the red triangles suggests the formation of QHSs with a filling factor $\nu^{gr}(= hn^{gr}/eB) \sim -2$, while the main peak centered at $V_g^{2D} = V_{CNP}^{2D}$ represents QHSs with the filling factor $\nu^{gr} \sim 0$. Note that R_{xx}^{gr} at $\nu^{gr} \sim -2$ remains a finite value even at $B \approx 8$ T, suggesting that the QHSs is not fully developed and our CVD graphene suffers from certain disorder. The disorder-induced density of states may contribute nonresonant photoresponse. To substantiate our claims, we extract n^{gr} associated with the valley (the red solid triangles) and the second peak (the red hollow squares) in Fig. 4(a) and display it as a function of B in Fig. 4(b). For comparison, a line of best fit through the data points corresponding to $\nu^{gr} = -2$ and -4 is also plotted in Fig. 4(b). It can be readily seen that the valley and the peak arise from $\nu^{gr} \sim -2$ and ~ -4, respectively. The uncertainty in the estimation of n^{gr} is the main source of the error bars. The second peak aside from the main peak at CNP is associated with the QHSs of $\nu^{gr} \sim -4$ for LL of $N = -1$ in graphene. It should be mentioned that by properly selecting capacitance $C \sim 113$ nF/cm^2 for $\nu^{gr} \sim -4$, and $C \sim 104$ nF/cm^2 for $\nu^{gr} \sim -2$, we can get the best-fit line. The fitted value of C is approximately 13% and 20% smaller than that of C_{GaAs} in the absence of the magnetic field. This discrepancy suggests that the capacitance of the hybrid graphene-2DEG material may depend on its electronic states and extra energy is required to reduce the total capacitance. For example, quantum capacitance C_Q, originating from the compressibility of 2DEG and acting in series with C_{GaAs}, is one of the possible sources to contribute such additional capacitance [26].

After identifying QHSs in graphene, we explore the photoresponse of graphene $\Delta R_{sig}^{gr}(= \Delta V_{xx}^{gr}/I^{gr})$ as a function of V_g^{2D}-V_{CNP}^{2D} at $T = 2$ K for various B, as shown in Fig. 4(c). A bias current I^{gr} of 500 nA on graphene optimizes the signal-to-noise ratio. The measurement setup is similar to that used in QHFIR detection. A positive ΔR_{sig}^{gr} is observed between $\nu^{gr} \sim -4$ and 0 as B exceeds 5.2 T, which gradually increases with increasing B. In contrast, a negative ΔR_{sig}^{gr} is found in the vicinity of the peak shoulders at $\nu^{gr} \sim 0$ and -4, which remains visible even when QHSs is not well resolved for $B < 5$ T. The negative ΔR_{sig}^{gr} has been observed in previous works [25,27,28]; however, the underlying mechanism is yet to be fully understood. In the control experiment, the mentioned features on ΔR_{sig}^{gr} disappear when the optical shutter is closed [see the green trace at $B = 8$ T, shown in Fig. 4(c)]. We hereby confirm that the observed ΔR_{sig}^{gr} is related to the bolometric effect, consistent with early reports [27,28]. The widespread photoresponse of ΔR_{sig}^{gr} in Fig. 4(c), e.g., trace at $B = 8$ T, can be understood by the broadening of LL. We note that early studies also observed fairly broad photoresponse, CR linewidth ~3 T at around 1000 cm^{-1} radiation, in the devices fabricated by exfoliated graphene [25]. On the other hand, CR linewidth in graphene on SiC is more like 0.1 T at similar probing energy [29,30]. It suggests that the CR linewidth broadening predominantly arises from surface effects associated with interactions between graphene and substrate-adatoms on the surface, which is moderately suppressed in devices deposited on SiC where the graphene layers are buried in few C-rich buffer layers on substrate. As for the hybrid graphene-2DEG device, in addition to the above-mentioned effect, the interplay between CVD graphene and metal LPA might be another source to cause the CR linewidth broadening. The photoresponse induced by nonresonant effects, e.g., ΔR_{sig}^{gr} at $\nu^{gr} \sim 0$ or independent of QHSs, is a broadband channel with no frequency selection. In contrast, early studies via LL spectroscopy have identified that the photoresponse around $\nu^{gr} \sim -4$ can be attributed to CR absorption [25,31]. As shown in Fig. 4(c), ΔR_{sig}^{gr} exhibits a declined shoulder around $\nu^{gr} \sim -4$, marked by the gray area, which substantially evolves with B and V_g^{2D}. Hence, we consider that ΔR_{sig}^{gr} near $\nu^{gr} \sim -4$ contains a tunable CR-related photoresponse. The performance merits of the graphene-based QHMIR detector is characterized by the R_v of ~13 V/W and the NEP of 3.8×10^{-9} W/Hz$^{1/2}$ [25,28].

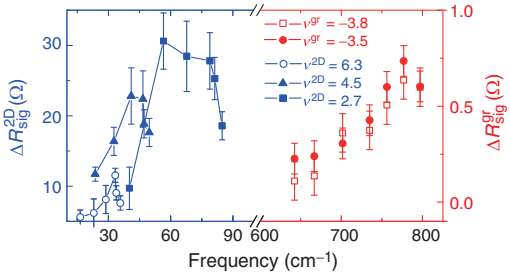

FIG. 5. The ΔR_{sig}^{2D} at $\nu^{2D} = 6.3$, 4.5, and 2.7 and ΔR_{sig}^{gr} at $\nu^{gr} = -3.8$ and -3.5 as a function of cyclotron frequency.

To summarize the dual-band photoresponse of the hybrid device as a function of the detection frequency, Fig. 5 shows ΔR_{sig}^{2D} at $\nu^{2D} = 6.3$, 4.5, and 2.7 and ΔR_{sig}^{gr} at $\nu^{gr} = -3.8$ and -3.5 as a function of ω_c^{2D} and ω_c^{gr}. The photoresponse of the 2DEG channel can be continuously tuned in FIR region from 24 to 89 cm^{-1}, whereas that of the graphene covers MIR region from 640–790 cm^{-1}. For comparison, characteristics of the hybrid QHIR photodetector and other graphene-based IR detectors are summarized in Table I.

Finally, we make a few comments on future improvement and development of the hybrid QHIR detector. First, although MIR photoresponse is observed in our QHMIR detector, higher-quality graphene is needed to further improve the device performance. A well-established technique is simply to prepare graphene on a hydrophobic substrate to alleviate the effect of charged impurities [34,35]. Second, the relatively low R_v of the QHMIR detector in Table I is mainly attributed to the low optical

TABLE I. Characteristics of the hybrid quantum Hall photodetctor and other graphene-based IR detectors, where R_v is the responsivity and $D^*(=A_s^{1/2}/\mathrm{NEP})$ is the specific detectivity.

	QHFIR	QHMIR	DGBLG-HEB[a]	GFET[b]
Material	GaAs/(Al, Ga)As	CVD graphene	Bilayer graphene	Exfoliated graphene
R_v (V/W)	8.2×10^4	13	2×10^5	0.1
D^* (cm $\mathrm{Hz}^{1/2}$/W)	1.1×10^9	1.1×10^6	···	···
Detection frequency (cm^{-1})	24–89	640–790	944	10
NEP ($\mathrm{nW/Hz}^{1/2}$)	1.4×10^{-2}	3.8	33×10^{-6}	200

[a]Dual-gated bilayer-graphene–hot-electron bolometer (DGBLG-HEB), from Ref. [32]. Note that R_v is estimated by using the absorbed power of graphene.
[b]Graphene field-effect-transistor- (GFET) based THz detector, from Ref. [33].

absorption of graphene [15,36], which would be a fundamental limitation by using the monolayer or few-layer 2D material for photosensing. To enhance light-matter coupling of graphene, one accessible route is to integrate plasmonic microstructures onto graphene [37–39]. Third, one may try to utilize interband CR transition to further extend the detector's response to higher energy photon and, more interestingly, exploit the Pauli-blocking effect to develop polarization-sensitive QHMIR detectors [29]. Finally, a variety of newly discovered 2D materials provide various alternatives for QHIR detection. Multiband IR detection could potentially be achieved by compositing these emergent materials and utilizing their QHSs. For example, distinct QHSs have been observed in black phosphorus [7] and MgZnO/ZnO heterostructures [9,40]. The electron effective mass is approximately $0.34m_0$ for black phosphorus and $1.17m_0$ for MgZnO/ZnO, which gives rise to a CR frequency of 0.8–6.3 cm^{-1} and 2.7–22 cm^{-1} for $1\ \mathrm{T} < B < 8\ \mathrm{T}$, respectively. Moreover, recent studies also suggest that LLs formed in the surface states of Bi-based topological insulators can be used for MIR detection at high temperatures (e.g., $T > 100$ K) [41,42].

V. CONCLUSION

In summary, we demonstrate a dual-band QHMIR-QHFIR photodetector based on the photoresponse induced by the CR absorption in a graphene-GaAs/(Al, Ga)As composite material. By operating 2DEG as a back-gate electrode, the graphene-QHMIR detector picks up a photosignal covering the frequency range of 640–790 cm^{-1}. Alternatively, using graphene as a top-gate electrode, the photoresponse range of the GaAs-QHFIR detector can be tuned over 24–89 cm^{-1}. Notably, our innovative design integrates a LPA to minimize the chip size and significantly enhance FIR detection. Our results pave a way for the development of a highly sensitive, tunable, multicolor quantum Hall MIR-FIR detector and imaging array.

ACKNOWLEDGMENTS

We acknowledge K. Hirakawa for the fruitful discussions with the experiment. This work was supported by Ministry of Science and Technology (MOST), Taiwan under Grants No. MOST 104-2112-M-007-010-MY3 and No. MOST 105-2811-M-007-096.

[1] E. L. Dereniak and G. D. Boreman, *Infrared Detectors and Systems* (Wiley-Interscience, New Jersey, 1996).
[2] Y. Kawano, Y. Hisanaga, H. Takenouchi, and S. Komiyama, Highly sensitive and tunable detection of far-infrared radiation by quantum Hall devices, J. Appl. Phys. **89**, 4037 (2001).
[3] N. G. Kalugin, Yu. B. Vasilyev, S. D. Suchalkin, G. Nachtwei, B. E. Sagol, and K. Eberl, Dynamics of the far-infrared photoresponse in quantum Hall systems, Phys. Rev. B **66**, 085308 (2002).
[4] Chiu-Chun Tang, D. C. Ling, C. C. Chi, and Jeng-Chung Chen, Highly tunable quantum Hall far-infrared photodetector by use of $\mathrm{GaAs/Al}_x\mathrm{Ga}_{1-x}\mathrm{As}$-graphene composite material, Appl. Phys. Lett. **105**, 181103 (2014).
[5] W. P. Halperin, The impact of helium shortages on basic research, Nat. Phys. **10**, 467 (2014).
[6] Yuanbo Zhang, Yan-Wen Tan, Horst L. Stormer, and Philip Kim, Experimental observation of the quantum Hall effect and Berry's phase in graphene, Nature (London) **438**, 201 (2005).
[7] Likai Li, Fangyuan Yang, Guo Jun Ye, Zuocheng Zhang, Zengwei Zhu, Wenkai Lou, Xiaoying Zhou, Liang Li, Kenji Watanabe, Takashi Taniguchi, Kai Chang, Yayu Wang, Xian Hui Chen, and Yuanbo Zhang, Quantum Hall effect in black phosphorus two-dimensional electron system, Nat. Nanotechnol. **11**, 593 (2016).
[8] Cui-Zu Chang *et al.*, Experimental observation of the quantum anomalous Hall effect in a magnetic topological insulator, Science **340**, 167 (2013).
[9] A. Tsukazaki, A. Ohtomo, T. Kita, Y. Ohno, H. Ohno, and M. Kawasaki, Quantum Hall effect in polar oxide heterostructures, Science **315**, 1388 (2007).
[10] F. H. L. Koppens, T. Mueller, Ph Avouris, A. C. Ferrari, M. S. Vitiello, and M. Polini, Photodetectors based on graphene, other two-dimensional materials and hybrid systems, Nat. Nanotechnol. **9**, 780 (2014).
[11] K. I. Bolotin, K. J. Sikes, Z. Jiang, M. Klima, G. Fudenberg, J. Hone, P. Kim, and H. L. Stormer, Ultrahigh electron mobility in suspended graphene, Solid State Commun. **146**, 351 (2008).

[12] T Mueller, F. Xia, and Ph. Avouris, Graphene photodetectors for high-speed optical communications, Nat. Photonics **4**, 297 (2010).

[13] Yukio Kawano, Wide-band frequency-tunable terahertz and infrared detection with graphene, Nanotechnology **24**, 214004 (2013).

[14] V. P. Gusynin, S. G. Sharapov, and J. P. Carbotte, Anomalous Absorption Line in the Magneto-Optical Response of Graphene, Phys. Rev. Lett. **98**, 157402 (2007).

[15] Z. Jiang, E. A. Henriksen, L. C. Tung, Y.-J. Wang, M. E. Schwartz, M. Y. Han, P. Kim, and H. L. Stormer, Infrared Spectroscopy of Landau Levels of Graphene, Phys. Rev. Lett. **98**, 197403 (2007).

[16] K. Takehana, Y. Imanaka, T. Takamasu, Y. Kim, and K.-S. An, Substrate dependence of cyclotron resonance on large-area CVD graphene, Curr. Appl. Phys. **14**, S119 (2014).

[17] Chiu-Chun Tang, Ming-Yang Li, L. J. Li, C. C. Chi, and Jeng-Chung Chen, Graphene-GaAs/$Al_xGa_{1-x}As$ heterostructure dual-function field-effect transistor, Appl. Phys. Lett. **101**, 202104 (2012).

[18] A. Das, S. Pisana, B. Charraborty, S. Piscanec, S. K. Saha, U. V. Waghmare, K. S. Novoselov, H. R. Krishnamurthy, A. K. Geim, A. C. Ferrari, and A. K. Sood, Monitoring dopants by Raman scattering in an electrochemically top-gated graphene transistor, Nat. Nanotechnol. **3**, 210 (2008).

[19] Kuan-Chun Lin, Ming-Yang Li, D. C. Ling, C. C. Chi, and Jeng-Chung Chen, Evolution of hot carrier dynamics in graphene with the Fermi level tuned across the Dirac point, Phys. Rev. B **91**, 125440 (2015).

[20] T. Mohamed Ali, N. Padmanathan, and S. Selladurai, Effect of nanofiller CeO_2 on structural, conductivity, and dielectric behaviors of plasticized blend nanocomposite polymer electrolyte, Ionics **21**, 829 (2015).

[21] K. Hirakawa, K. Yamanaka, Y. Kawaguchi, M. Endo, M. Saeki, and S. Komiyama, Far-infrared photoresponse of the magnetoresistance of the two-dimensional electron systems in the integer quantized Hall regime, Phys. Rev. B **63**, 085320 (2001).

[22] Y. Kawaguchi, K. Hirakawa, and S. Komiyama, High-sensitivity quantum Hall far-infrared photodetector integrated with log-periodic antenna, Appl. Phys. Lett. **80**, 3418 (2002).

[23] Chiu-Chun Tang, Ming-Yang Li, L. J. Li, C. C. Chi, and J. C. Chen, Characteristics of a sensitive micro-Hall probe fabricated on chemical vapor deposited graphene over the temperature range from liquid-helium to room temperature, Appl. Phys. Lett. **99**, 112107 (2011).

[24] Jeng-Chung Chen, Jingbin Zhang, Cheng-Chung Chi, Takeji Ueda, and Susumu Komiyama, Temperature limitations of quantum Hall far-infrared photodetectors, Jpn. J. Appl. Phys. **49**, 031201 (2010).

[25] R. S. Deacon, K.-C. Chuang, R. J. Nicholas, K. S. Novoselov, and A. K. Geim, Cyclotron resonance study of the electron and hole velocity in graphene monolayers, Phys. Rev. B **76**, 081406 (2007).

[26] G. L. Yu, R. Jalil, Branson Belle, Alexander S. Mayorov, Peter Blake, Frederick Schedin, Sergey V. Morozov, Leonid A. Ponomarenko, F. Chiappini, S. Wiedmann, Uli Zeitler, Mikhail I. Katsnelson, A. K. Geim, Kostya S. Novoselov, and Daniel C. Elias, Interaction phenomena in graphene seen through quantum capacitance, Proc. Natl. Acad. Sci. U.S.A. **110**, 3282 (2013).

[27] Nikolai G. Kalugin, Lei Lei Jing, Wenzhong Bao, Lee Wickey, Christopher Del Barga, Mekan Ovezmyradov, Eric A. Shaner, and Chun Ning Lau, Graphene-based quantum Hall effect infrared photodetector operating at liquid nitrogen temperatures, Appl. Phys. Lett. **99**, 013504 (2011).

[28] Satoru Masubuchi, Masahiro Onuki, Miho Arai, Takehiro Yamaguchi, Kenji Watanabe, Takashi Taniguchi, and Tomoki Machida, Photovoltaic infrared photoresponse of the high-mobility graphene quantum Hall system due to cyclotron resonance, Phys. Rev. B **88**, 121402 (2013).

[29] Chase T. Ellis, Andreas V. Stier, Myoung-Hwan Kim, Joseph G. Tischler, Evan R. Glaser, Rachael L. Myers-Ward, Joseph L. Tedesco, Charles R. Eddy, D. Kurt Gaskill, and John Cerne, Magneto-optical fingerprints of distinct graphene multilayers using the giant infrared Kerr effect, Sci. Rep. **3**, 3143 (2013).

[30] P. Kühne, V. Darakchieva, R. Yakimova, J. D. Tedesco, R. L. Myers-Ward, C. R. Eddy, D. K. Gaskill, C. M. Herzinger, J. A. Woollam, M. Schubert, and T. Hofmann, Polarization Selection Rules for Inter-Landau-Level Transitions in Epitaxial Graphene Revealed by the Infrared Optical Hall Effect, Phys. Rev. Lett. **111**, 077402 (2013).

[31] Kai-Chieh Chuang, Russell S. Deacon, Robin J. Nicholas, Kostya S. Novoselov, and Andre K. Geim, Cyclotron resonance of electrons and holes in graphene monolayers, Phil. Trans. R. Soc. A **366**, 237 (2008).

[32] Jun Yan, M. H. Kim, J. A. Elle, A. B. Sushkov, G. S. Jenkins, H. M. Milchberg, M. S. Fuhrer, and H. D. Drew, Dual-gated bilayer graphene hot-electron bolometer, Nat. Nanotechnol. **7**, 472 (2012).

[33] L. Vicarelli, M. S. Vitiello, D. Coquillat, A. Lombardo, A. C. Ferrari, W. Knap, M. Polini, V. Pellegrini, and A. Tredicucci, Graphene field-effect transistors as room-temperature terahertz detectors, Nat. Mater. **11**, 865 (2012).

[34] Myrsini Lafkioti, Benjamin Krauss, Timm Lohmann, Ute Zschieschang, Hagen Klauk, Klaus v. Klitzing, and Jurgen H. Smet, Graphene on a hydrophobic substrate: Doping reduction and hysteresis suppression under ambient conditions, Nano Lett. **10**, 1149 (2010).

[35] C. R. Dean, A. F. Young, I. Meric, C. Lee, L. Wang, S. Sorgenfrei, K. Watanabe, T. Taniguchi, P. Kim, K. L. Shepard, and J. Hone, Boron nitride substrates for high-quality graphene electronics, Nat. Nanotechnol. **5**, 722 (2010).

[36] R. R. Nair, P. Blake, A. N. Grigorenko, K. S. Novoselov, T. J. Booth, T. Stauber, N. M. R. Peres, and A. K. Geim, Fine structure constant defines visual transparency of graphene, Science **320**, 1308 (2008).

[37] T. J. Echtermeyer, L. Britnell, P. K. Jasnos, A. Lombardo, R. V. Gorbachev, A. N. Grigorenko, A. K. Geim, A. C. Ferrari, and K. S. Novoselov, Strong plasmonic enhancement of photovoltage in graphene, Nat. Commun. **2**, 458 (2011).

[38] Yue Su, Zhongxun Guo, Wen Huang, Zhiwei Liu, Tianxun Gong, Yiwen He, and Bin Yu, Ultra-sensitive graphene photodetector with plasmonic structure, Appl. Phys. Lett. **109**, 173107 (2016).

[39] A. N. Grigorenko, M. Polini, and K. S. Novoselov, Graphene plasmonics, Nat. Photonics **6**, 749 (2012).

[40] A. Tsukazaki, S. Akasaka, K. Nakahara, Y. Ohno, H. Ohno, D. Maryenko, A. Ohtomo, and M. Kawasaki, Observation of the fractional quantum Hall effect in an oxide, Nat. Mater. **9**, 889 (2010).

[41] A. A. Schafgans, K. W. Post, A. A. Taskin, Yoichi Ando, Xiao-Liang Qi, B. C. Chapler, and D. N. Basov, Landau level spectroscopy of surface states in the topological insulator $Bi_{0.91}Sb_{0.09}$ via magneto-optics, Phys. Rev. B **85**, 195440 (2012).

[42] R. Yoshimi, A. Tsukazaki, K. Kikutake, J. G. Checkelsky, K. S. Takahashi, M. Kawasaki, and Y. Tokura, Dirac electron states formed at the heterointerface between a topological insulator and a conventional semiconductor, Nat. Mater. **13**, 253 (2014).